Research Article | Vol. 26, No. 6 | 19 Mar 2018 | OPTICS EXPRESS 7270
Optics EXPRESS

Point-spread function manipulation of the swept-source optical coherence tomography through temporal phase modulation

CHI ZHANG,[1,2] RUI ZHU,[3] AND KENNETH K. Y. WONG[2,*]

[1]*Wuhan National Laboratory for Optoelectronics, Huazhong University of Science and Technology, 1037 Luoyu Road, Wuhan, China*
[2]*Photonic Systems Research Laboratory, Department of Electrical and Electronic Engineering, The University of Hong Kong, Pokfulam Road, Hong Kong, China*
[3]*Shenzhen Vivolight Medical Devices & Technology Co., Ltd, Shenzhen, China*
[*]*kywong@eee.hku.hk*

Abstract: Recent breakthroughs in microscopy have surpassed Abbe's spatial diffraction limit, especially in the regime of fluorescence imaging. Microcopy's depth-imaging relative tomography is, however, still confined to basic imaging quality, which is limited by the Fourier bandwidth. In this paper, we explore the analogy between spatial microscopy and temporal tomography based on the space-time duality, and hence enlighten the advancement of tomography. As a proof-of-principle demonstration, an all-optical manipulation of the point-spread function (PSF) of a swept-source optical coherence tomography (OCT) is performed based on temporal phase modulation. Although the axial resolving power remains the same, much sharper sketch lines can be obtained from the specimen. In addition, the imaging quality is also improved with suppressed ghost fringes and better sensitivity.

OCIS codes: (100.2980) Image enhancement; (110.4500) Optical coherence tomography; (120.5060) Phase modulation.

References and links

1. G. N. Hounsfield, "Computerized transverse axial scanning (tomography).Part 1. Description of system," Br. J. Radiol. **46**(552), 1016–1022 (1973).
2. J. J. Wild and J. M. Reid, "Application of Echo-Ranging Techniques to the Determination of Structure of Biological Tissues," Science **115**(2983), 226–230 (1952).
3. B. P. Abbott, R. Abbott, T. D. Abbott, M. R. Abernathy, F. Acernese, K. Ackley, C. Adams, T. Adams, P. Addesso, R. X. Adhikari, V. B. Adya, C. Affeldt, M. Agathos, K. Agatsuma, N. Aggarwal, O. D. Aguiar, L. Aiello, A. Ain, P. Ajith, B. Allen, A. Allocca, P. A. Altin, S. B. Anderson, W. G. Anderson, K. Arai, M. A. Arain, M. C. Araya, C. C. Arceneaux, J. S. Areeda, N. Arnaud, K. G. Arun, S. Ascenzi, G. Ashton, M. Ast, S. M. Aston, P. Astone, P. Aufmuth, C. Aulbert, S. Babak, P. Bacon, M. K. Bader, P. T. Baker, F. Baldaccini, G. Ballardin, S. W. Ballmer, J. C. Barayoga, S. E. Barclay, B. C. Barish, D. Barker, F. Barone, B. Barr, L. Barsotti, M. Barsuglia, D. Barta, J. Bartlett, M. A. Barton, I. Bartos, R. Bassiri, A. Basti, J. C. Batch, C. Baune, V. Bavigadda, M. Bazzan, B. Behnke, M. Bejger, C. Belczynski, A. S. Bell, C. J. Bell, B. K. Berger, J. Bergman, G. Bergmann, C. P. Berry, D. Bersanetti, A. Bertolini, J. Betzwieser, S. Bhagwat, R. Bhandare, I. A. Bilenko, G. Billingsley, J. Birch, R. Birney, O. Birnholtz, S. Biscans, A. Bisht, M. Bitossi, C. Biwer, M. A. Bizouard, J. K. Blackburn, C. D. Blair, D. G. Blair, R. M. Blair, S. Bloemen, O. Bock, T. P. Bodiya, M. Boer, G. Bogaert, C. Bogan, A. Bohe, P. Bojtos, C. Bond, F. Bondu, R. Bonnand, B. A. Boom, R. Bork, V. Boschi, S. Bose, Y. Bouffanais, A. Bozzi, C. Bradaschia, P. R. Brady, V. B. Braginsky, M. Branchesi, J. E. Brau, T. Briant, A. Brillet, M. Brinkmann, V. Brisson, P. Brockill, A. F. Brooks, D. A. Brown, D. D. Brown, N. M. Brown, C. C. Buchanan, A. Buikema, T. Bulik, H. J. Bulten, A. Buonanno, D. Buskulic, C. Buy, R. L. Byer, M. Cabero, L. Cadonati, G. Cagnoli, C. Cahillane, J. Calderón Bustillo, T. Callister, E. Calloni, J. B. Camp, K. C. Cannon, J. Cao, C. D. Capano, E. Capocasa, F. Carbognani, S. Caride, J. Casanueva Diaz, C. Casentini, S. Caudill, M. Cavaglià, F. Cavalier, R. Cavalieri, G. Cella, C. B. Cepeda, L. Cerboni Baiardi, G. Cerretani, E. Cesarini, R. Chakraborty, T. Chalermsongsak, S. J. Chamberlin, M. Chan, S. Chao, P. Charlton, E. Chassande-Mottin, H. Y. Chen, Y. Chen, C. Cheng, A. Chincarini, A. Chiummo, H. S. Cho, M. Cho, J. H. Chow, N. Christensen, Q. Chu, S. Chua, S. Chung, G. Ciani, F. Clara, J. A. Clark, F. Cleva, E. Coccia, P. F. Cohadon, A. Colla, C. G. Collette, L. Cominsky, M. Constancio, Jr., A. Conte, L. Conti, D. Cook, T. R. Corbitt, N. Cornish, A. Corsi, S. Cortese, C. A. Costa, M. W. Coughlin, S. B. Coughlin, J. P. Coulon, S. T. Countryman, P. Couvares, E. E. Cowan, D. M. Coward, M. J. Cowart, D. C. Coyne, R. Coyne, K. Craig, J. D. Creighton, T. D. Creighton, J. Cripe, S. G. Crowder, A. M. Cruise, A. Cumming, L. Cunningham, E. Cuoco, T. Dal Canton, S. L. Danilishin, S. D'Antonio, K. Danzmann, N. S. Darman, C. F. Da Silva Costa, V. Dattilo, I. Dave, H. P. Daveloza, M. Davier, G. S. Davies, E. J. Daw, R. Day, S. De, D. DeBra, G. Debreczeni, J. Degallaix, M. De Laurentis, S. Deléglise, W. Del Pozzo,

#318403 https://doi.org/10.1364/OE.26.007270
Journal © 2018 Received 27 Dec 2017; revised 7 Mar 2018; accepted 7 Mar 2018; published 12 Mar 2018

Optics EXPRESS

T. Denker, T. Dent, H. Dereli, V. Dergachev, R. T. DeRosa, R. De Rosa, R. DeSalvo, S. Dhurandhar, M. C. Díaz, L. Di Fiore, M. Di Giovanni, A. Di Lieto, S. Di Pace, I. Di Palma, A. Di Virgilio, G. Dojcinoski, V. Dolique, F. Donovan, K. L. Dooley, S. Doravari, R. Douglas, T. P. Downes, M. Drago, R. W. Drever, J. C. Driggers, Z. Du, M. Ducrot, S. E. Dwyer, T. B. Edo, M. C. Edwards, A. Effler, H. B. Eggenstein, P. Ehrens, J. Eichholz, S. S. Eikenberry, W. Engels, R. C. Essick, T. Etzel, M. Evans, T. M. Evans, R. Everett, M. Factourovich, V. Fafone, H. Fair, S. Fairhurst, X. Fan, Q. Fang, S. Farinon, B. Farr, W. M. Farr, M. Favata, M. Fays, H. Fehrmann, M. M. Fejer, D. Feldbaum, I. Ferrante, E. C. Ferreira, F. Ferrini, F. Fidecaro, L. S. Finn, I. Fiori, D. Fiorucci, R. P. Fisher, R. Flaminio, M. Fletcher, H. Fong, J. D. Fournier, S. Franco, S. Frasca, F. Frasconi, M. Frede, Z. Frei, A. Freise, R. Frey, V. Frey, T. T. Fricke, P. Fritschel, V. V. Frolov, P. Fulda, M. Fyffe, H. A. Gabbard, J. R. Gair, L. Gammaitoni, S. G. Gaonkar, F. Garufi, A. Gatto, G. Gaur, N. Gehrels, G. Gemme, B. Gendre, E. Genin, A. Gennai, J. George, L. Gergely, V. Germain, A. Ghosh, A. Ghosh, S. Ghosh, J. A. Giaime, K. D. Giardina, A. Giazotto, K. Gill, A. Glaefke, J. R. Gleason, E. Goetz, R. Goetz, L. Gondan, G. González, J. M. Gonzalez Castro, A. Gopakumar, N. A. Gordon, M. L. Gorodetsky, S. E. Gossan, M. Gosselin, R. Gouaty, C. Graef, P. B. Graff, M. Granata, A. Grant, S. Gras, C. Gray, G. Greco, A. C. Green, R. J. Greenhalgh, P. Groot, H. Grote, S. Grunewald, G. M. Guidi, X. Guo, A. Gupta, M. K. Gupta, K. E. Gushwa, E. K. Gustafson, R. Gustafson, J. J. Hacker, B. R. Hall, E. D. Hall, G. Hammond, M. Haney, M. M. Hanke, J. Hanks, C. Hanna, M. D. Hannam, J. Hanson, T. Hardwick, J. Harms, G. M. Harry, I. W. Harry, M. J. Hart, M. T. Hartman, C. J. Haster, K. Haughian, J. Healy, J. Heefner, A. Heidmann, M. C. Heintze, G. Heinzel, H. Heitmann, P. Hello, G. Hemming, M. Hendry, I. S. Heng, J. Hennig, A. W. Heptonstall, M. Heurs, S. Hild, D. Hoak, K. A. Hodge, D. Hofman, S. E. Hollitt, K. Holt, D. E. Holz, P. Hopkins, D. J. Hosken, J. Hough, E. A. Houston, E. J. Howell, Y. M. Hu, S. Huang, E. A. Huerta, D. Huet, B. Hughey, S. Husa, S. H. Huttner, T. Huynh-Dinh, A. Idrisy, N. Indik, D. R. Ingram, R. Inta, H. N. Isa, J. M. Isac, M. Isi, G. Islas, T. Isogai, B. R. Iyer, K. Izumi, M. B. Jacobson, T. Jacqmin, H. Jang, K. Jani, P. Jaranowski, S. Jawahar, F. Jiménez-Forteza, W. W. Johnson, N. K. Johnson-McDaniel, D. I. Jones, R. Jones, R. J. Jonker, L. Ju, K. Haris, C. V. Kalaghatgi, V. Kalogera, S. Kandhasamy, G. Kang, J. B. Kanner, S. Karki, M. Kasprzack, E. Katsavounidis, W. Katzman, S. Kaufer, T. Kaur, K. Kawabe, F. Kawazoe, F. Kéfélian, M. S. Kehl, D. Keitel, D. B. Kelley, W. Kells, R. Kennedy, D. G. Keppel, J. S. Key, A. Khalaidovski, F. Y. Khalili, I. Khan, S. Khan, Z. Khan, E. A. Khazanov, N. Kijbunchoo, C. Kim, J. Kim, K. Kim, N. G. Kim, N. Kim, Y. M. Kim, E. J. King, P. J. King, D. L. Kinzel, J. S. Kissel, L. Kleybolte, S. Klimenko, S. M. Koehlenbeck, K. Kokeyama, S. Koley, V. Kondrashov, A. Kontos, S. Koranda, M. Korobko, W. Z. Korth, I. Kowalska, D. B. Kozak, V. Kringel, B. Krishnan, A. Królak, C. Krueger, G. Kuehn, P. Kumar, R. Kumar, L. Kuo, A. Kutynia, P. Kwee, B. D. Lackey, M. Landry, J. Lange, B. Lantz, P. D. Lasky, A. Lazzarini, C. Lazzaro, P. Leaci, S. Leavey, E. O. Lebigot, C. H. Lee, H. K. Lee, H. M. Lee, K. Lee, A. Lenon, M. Leonardi, J. R. Leong, N. Leroy, N. Letendre, Y. Levin, B. M. Levine, T. G. Li, A. Libson, T. B. Littenberg, N. A. Lockerbie, J. Logue, A. L. Lombardi, L. T. London, J. E. Lord, M. Lorenzini, V. Loriette, M. Lormand, G. Losurdo, J. D. Lough, C. O. Lousto, G. Lovelace, H. Lück, A. P. Lundgren, J. Luo, R. Lynch, Y. Ma, T. MacDonald, B. Machenschalk, M. MacInnis, D. M. Macleod, F. Magaña-Sandoval, R. M. Magee, M. Mageswaran, E. Majorana, I. Maksimovic, V. Malvezzi, N. Man, I. Mandel, V. Mandic, V. Mangano, G. L. Mansell, M. Manske, M. Mantovani, F. Marchesoni, F. Marion, S. Márka, Z. Márka, A. S. Markosyan, E. Maros, F. Martelli, L. Martellini, I. W. Martin, R. M. Martin, D. V. Martynov, J. N. Marx, K. Mason, A. Masserot, T. J. Massinger, M. Masso-Reid, F. Matichard, L. Matone, N. Mavalvala, N. Mazumder, G. Mazzolo, R. McCarthy, D. E. McClelland, S. McCormick, S. C. McGuire, G. McIntyre, J. McIver, D. J. McManus, S. T. McWilliams, D. Meacher, G. D. Meadors, J. Meidam, A. Melatos, G. Mendell, D. Mendoza-Gandara, R. A. Mercer, E. Merilh, M. Merzougui, S. Meshkov, C. Messenger, C. Messick, P. M. Meyers, F. Mezzani, H. Miao, C. Michel, H. Middleton, E. E. Mikhailov, L. Milano, J. Miller, M. Millhouse, Y. Minenkov, J. Ming, S. Mirshekari, C. Mishra, S. Mitra, V. P. Mitrofanov, G. Mitselmakher, R. Mittleman, A. Moggi, M. Mohan, S. R. Mohapatra, M. Montani, B. C. Moore, C. J. Moore, D. Moraru, G. Moreno, S. R. Morriss, K. Mossavi, B. Mours, C. M. Mow-Lowry, C. L. Mueller, G. Mueller, A. W. Muir, A. Mukherjee, D. Mukherjee, S. Mukherjee, N. Mukund, A. Mullavey, J. Munch, D. J. Murphy, P. G. Murray, A. Mytidis, I. Nardecchia, L. Naticchioni, R. K. Nayak, V. Necula, K. Nedkova, G. Nelemans, M. Neri, A. Neunzert, G. Newton, T. T. Nguyen, A. B. Nielsen, S. Nissanke, A. Nitz, F. Nocera, D. Nolting, M. E. Normandin, L. K. Nuttall, J. Oberling, E. Ochsner, J. O'Dell, E. Oelker, G. H. Ogin, J. J. Oh, S. H. Oh, F. Ohme, M. Oliver, P. Oppermann, R. J. Oram, B. O'Reilly, R. O'Shaughnessy, C. D. Ott, D. J. Ottaway, R. S. Ottens, H. Overmier, B. J. Owen, A. Pai, S. A. Pai, J. R. Palamos, O. Palashov, C. Palomba, A. Pal-Singh, H. Pan, Y. Pan, C. Pankow, F. Pannarale, B. C. Pant, F. Paoletti, A. Paoli, M. A. Papa, H. R. Paris, W. Parker, D. Pascucci, A. Pasqualetti, R. Passaquieti, D. Passuello, B. Patricelli, Z. Patrick, B. L. Pearlstone, M. Pedraza, R. Pedurand, L. Pekowsky, A. Pele, S. Penn, A. Perreca, H. P. Pfeiffer, M. Phelps, O. Piccinni, M. Pichot, M. Pickenpack, F. Piergiovanni, V. Pierro, G. Pillant, L. Pinard, I. M. Pinto, M. Pitkin, J. H. Poeld, R. Poggiani, P. Popolizio, A. Post, J. Powell, J. Prasad, V. Predoi, S. S. Premachandra, T. Prestegard, L. R. Price, M. Prijatelj, M. Principe, S. Privitera, R. Prix, G. A. Prodi, L. Prokhorov, O. Puncken, M. Punturo, P. Puppo, M. Pürrer, H. Qi, J. Qin, V. Quetschke, E. A. Quintero, R. Quitzow-James, F. J. Raab, D. S. Rabeling, H. Radkins, P. Raffai, S. Raja, M. Rakhmanov, C. R. Ramet, P. Rapagnani, V. Raymond, M. Razzano, V. Re, J. Read, C. M. Reed, T. Regimbau, L. Rei, S. Reid, D. H. Reitze, H. Rew, S. D. Reyes, F. Ricci, K. Riles, N. A. Robertson, R. Robie, F. Robinet, A. Rocchi, L. Rolland, J. G. Rollins, V. J. Roma, J. D. Romano, R. Romano, G. Romanov, J. H. Romie, D. Rosińska, S. Rowan, A. Rüdiger, P. Ruggi, K. Ryan, S. Sachdev, T. Sadecki, L. Sadeghian, L. Salconi, M. Saleem, F. Salemi, A. Samajdar, L. Sammut, L. M. Sampson, E. J. Sanchez, V. Sandberg, B. Sandeen, G. H. Sanders, J. R. Sanders, B. Sassolas, B. S. Sathyaprakash, P. R. Saulson, O. Sauter, R. L. Savage, A. Sawadsky, P. Schale, R. Schilling, J. Schmidt, P. Schmidt, R. Schnabel, R. M. Schofield, A. Schönbeck, E. Schreiber, D. Schuette, B. F. Schutz, J. Scott, S. M. Scott, D. Sellers, A. S. Sengupta, D. Sentenac, V. Sequino, A. Sergeev, G. Serna, Y. Setyawati, A. Sevigny, D.

Optics EXPRESS

A. Shaddock, T. Shaffer, S. Shah, M. S. Shahriar, M. Shaltev, Z. Shao, B. Shapiro, P. Shawhan, A. Sheperd, D. H. Shoemaker, D. M. Shoemaker, K. Siellez, X. Siemens, D. Sigg, A. D. Silva, D. Simakov, A. Singer, L. P. Singer, A. Singh, R. Singh, A. Singhal, A. M. Sintes, B. J. Slagmolen, J. R. Smith, M. R. Smith, N. D. Smith, R. J. Smith, E. J. Son, B. Sorazu, F. Sorrentino, T. Souradeep, A. K. Srivastava, A. Staley, M. Steinke, J. Steinlechner, S. Steinlechner, D. Steinmeyer, B. C. Stephens, S. P. Stevenson, R. Stone, K. A. Strain, N. Straniero, G. Stratta, N. A. Strauss, S. Strigin, R. Sturani, A. L. Stuver, T. Z. Summerscales, L. Sun, P. J. Sutton, B. L. Swinkels, M. J. Szczepańczyk, M. Tacca, D. Talukder, D. B. Tanner, M. Tápai, S. P. Tarabrin, A. Taracchini, R. Taylor, T. Theeg, M. P. Thirugnanasambandam, E. G. Thomas, M. Thomas, P. Thomas, K. A. Thorne, K. S. Thorne, E. Thrane, S. Tiwari, V. Tiwari, K. V. Tokmakov, C. Tomlinson, M. Tonelli, C. V. Torres, C. I. Torrie, D. Töyrä, F. Travasso, G. Traylor, D. Trifirò, M. C. Tringali, L. Trozzo, M. Tse, M. Turconi, D. Tuyenbayev, D. Ugolini, C. S. Unnikrishnan, A. L. Urban, S. A. Usman, H. Vahlbruch, G. Vajente, G. Valdes, M. Vallisneri, N. van Bakel, M. van Beuzekom, J. F. van den Brand, C. Van Den Broeck, D. C. Vander-Hyde, L. van der Schaaf, J. V. van Heijningen, A. A. van Veggel, M. Vardaro, S. Vass, M. Vasúth, R. Vaulin, A. Vecchio, G. Vedovato, J. Veitch, P. J. Veitch, K. Venkateswara, D. Verkindt, F. Vetrano, A. Viceré, S. Vinciguerra, D. J. Vine, J. Y. Vinet, S. Vitale, T. Vo, H. Vocca, C. Vorvick, D. Voss, W. D. Vousden, S. P. Vyatchanin, A. R. Wade, L. E. Wade, M. Wade, S. J. Waldman, M. Walker, L. Wallace, S. Walsh, G. Wang, H. Wang, M. Wang, X. Wang, Y. Wang, H. Ward, R. L. Ward, J. Warner, M. Was, B. Weaver, L. W. Wei, M. Weinert, A. J. Weinstein, R. Weiss, T. Welborn, L. Wen, P. Weßels, T. Westphal, K. Wette, J. T. Whelan, S. E. Whitcomb, D. J. White, B. F. Whiting, K. Wiesner, C. Wilkinson, P. A. Willems, L. Williams, R. D. Williams, A. R. Williamson, J. L. Willis, B. Willke, M. H. Wimmer, L. Winkelmann, W. Winkler, C. C. Wipf, A. G. Wiseman, H. Wittel, G. Woan, J. Worden, J. L. Wright, G. Wu, J. Yablon, I. Yakushin, W. Yam, H. Yamamoto, C. C. Yancey, M. J. Yap, H. Yu, M. Yvert, A. Zadrożny, L. Zangrando, M. Zanolin, J. P. Zendri, M. Zevin, F. Zhang, L. Zhang, M. Zhang, Y. Zhang, C. Zhao, M. Zhou, Z. Zhou, X. J. Zhu, M. E. Zucker, S. E. Zuraw, and J. Zweizig; LIGO Scientific Collaboration and Virgo Collaboration, "Observation of Gravitational Waves from a Binary Black Hole Merger," Phys. Rev. Lett. **116**(6), 061102 (2016).

4. D. Huang, E. Swanson, C. Lin, J. Schuman, W. Stinson, W. Chang, M. Hee, T. Flotte, K. Gregory, C. Puliafito, and J. G. Fujimoto, "Optical Coherence Tomography," Science **254**(5035), 1178–1181 (1991).
5. A. F. Fercher, C. K. Hitzenberger, G. Kamp, and S. Y. El-Zaiat, "Measurement of intraocular distances by backscattering spectral interferometry," Opt. Commun. **117**(1-2), 43–48 (1995).
6. T. Klein, W. Wieser, L. Reznicek, A. Neubauer, A. Kampik, and R. Huber, "Multi-MHz retinal OCT," Biomed. Opt. Express **4**(10), 1890–1908 (2013).
7. M. Siddiqui, A. S. Nam, S. Tozburun, N. Lippok, C. Blatter, and B. J. Vakoc, "High-speed optical coherence tomography by circular interferometric ranging," Nat. Photonics **12**(2), 111–116 (2018).
8. L. M. Manojlovic, "Novel Method for Optical Coherence Tomography Resolution Enhancement," IEEE J. Quantum Electron. **47**(3), 340–347 (2011).
9. M. D. Kulkarni, C. W. Thomas, and J. A. Izatt, "Image enhancement in optical coherence tomography using deconvolution," Electron. Lett. **33**(16), 1365–1367 (1997).
10. M. Born and E. Wolf, *Principles of Optics* (Cambridge University, 1999).
11. S. W. Hell and J. Wichmann, "Breaking the diffraction resolution limit by stimulated emission: stimulated-emission-depletion fluorescence microscopy," Opt. Lett. **19**(11), 780–782 (1994).
12. T. A. Klar, S. Jakobs, M. Dyba, A. Egner, and S. W. Hell, "Fluorescence microscopy with diffraction resolution barrier broken by stimulated emission," Proc. Natl. Acad. Sci. U.S.A. **97**(15), 8206–8210 (2000).
13. J. W. Goodman, *Introduction to Fourier Optics* 2nd ed. (The McGraw-Hill Companies, Inc. 1996).
14. B. H. Kolner, "Space-Time Duality and the Theory of Temporal Imaging," IEEE J. Quantum Electron. **30**(8), 1951–1963 (1994).
15. M. A. Foster, R. Salem, D. F. Geraghty, A. C. Turner-Foster, M. Lipson, and A. L. Gaeta, "Silicon-chip-based ultrafast optical oscilloscope," Nature **456**(7218), 81–84 (2008).
16. C. Zhang, J. Xu, P. C. Chui, and K. K. Y. Wong, "Parametric spectro-temporal analyzer (PASTA) for real-time optical spectrum observation," Sci. Rep. **3**(1), 2064 (2013).
17. C. Zhang, X. Wei, M. E. Marhic, and K. K. Y. Wong, "Ultrafast and versatile spectroscopy by temporal Fourier transform," Sci. Rep. **4**, 5351 (2014).
18. C. Zhang and K. K. Y. Wong, "Wavelength-encoded tomography based on optical temporal Fourier transform," Appl. Phys. Lett. **105**(9), 091109 (2014).
19. P. H. Tomlins and R. K. Wang, "Theory, developments and applications of optical coherence tomography," J. Phys. D Appl. Phys. **38**(15), 2519–2535 (2005).
20. High speed 1310nm swept source for OCT, http://www.axsun.com/oct-swept-lasers (Accessed Dec. 27, 2017).
21. M. Martinez-Corral, M. Caballero, E. H. K. Stelzer, and J. Swoger, "Tailoring the axial shape of the point spread function using the Toraldo concept," Opt. Express **10**(1), 98–103 (2002).

1. Introduction

Absolute distance measurement by the reflective interferometry can achieve ultrahigh resolution, especially the optical modalities, owing to its short wavelength range over the ultrasound counterparts [1,2]. Such as the gravitational waves were observed by advanced laser interferometer gravitational-wave observatory (advanced LIGO) recently, which achieved as high as 10^{-15} m distance accuracy [3]. Another laser interferometer based imaging

Optics EXPRESS

modality, optical coherence tomography (OCT) has proven to be a powerful non-invasive cross-sectional imaging modality, and it is advantageous in terms of both axial and lateral resolution. As in the early stage time-domain OCT, each axial A-line required the mechanical scanning of the reference mirror over one period of time, which resulted in a poor frame rate [4]. Later, the Fourier-domain OCT improved the frame rate by resolving the interference fringes in the frequency domain [5], and the more recent swept-source OCT has realized a record megahertz A-scan rate [6,7]. Some computational strategies, e.g. spectral shaping [8] or deconvolution [9], have been reported to optimize the point spread function (PSF), and achieve sharper boundaries, but its axial resolving power is still bounded by the limited spectral bandwidth.

Similar situation was encountered in observing Abbe's diffraction limit by microscopy, where the resolving power is bounded by the wavelength and the inverse of the numerical aperture (NA) of the objective lens [10]. With the emergence of the fluorescence microscope, numerous super-resolution techniques arose by manipulating the PSFs of these point-imaging systems, such as the stimulated emission depletion (STED) microscopy, which revolutionized optical microscopy into the nanometer-dimension [11,12]. It is noted that, this PSF manipulation enabled super-resolution is based on the point-imaging condition. According to the space-time duality, there is a mathematic analogy between the spatial microscopy and temporal tomography (see appendix I for more detailed analysis) [13,14]. Ideally, optical temporal Fourier transformation is implemented by the time-lens focusing mechanism, which has been applied in the ultrafast oscilloscope or spectroscopy [15–17]. However, most of the existing OCT systems still directly capture the frequency interference fringes, and retrieve the depth information by Fourier transformation in the electrical domain instead of the optical domain [18]. Owing to the diffraction of light, the resolution of optical microscopy is limited by its NA in the spatial domain [10]. Similarly, for its temporal counterpart tomography, the resolution is limited by the spectral bandwidth [19]. To enhance the minimum resolvable points in the spatial domain, the original excited diffraction-limited PSF is compressed by introducing a doughnut-shaped depletion field [11]. In the work [11], the most essential part is to introduce a spatial π-stepped phase mask to generate the doughnut-shaped PSF. By adapting this concept in the time domain (especially for swept-source OCT, which linearly maps the spectral information in the time domain), the spatial phase mask will become a temporal phase modulator, and a subtraction will replace the depletion process [14]. However, this PSF manipulation cannot help to improve the resolution, since OCT is a line imaging system, and the compressed PSF will be affected and merged with the neighboring pulse during the subtraction process.

In this paper, the PSF sidelobe suppression of the swept-source OCT is carried out. Although the axial resolving power still remains the same due to the spectral bandwidth limit, the sketch lines enhancement is observed from the real sample, and the isolated single layer pulsewidth is compressed from 20 μm to 4 μm, which can be viewed as the sidelobe suppression of the PSF. This single layer pulsewidth is different from the axial resolution, since the adjacent multiple-layer PSF does not work based on this PSF sidelobe suppression scheme, which will be discussed in detail in the later part. Moreover, similar to the balanced detection (BD) technology, the suppression of the ghost fringes and the sensitivity enhancement is also achieved based on this PSF sidelobe suppression scheme with single detector, and these two schemes are easily compatible with each other. It is promising that, this PSF sidelobe suppression scheme is able to break the axial resolving power limit, as long as the OCT imaging modality is configured as a point-imaging system.

Optics EXPRESS

2. Principles and experimental setup

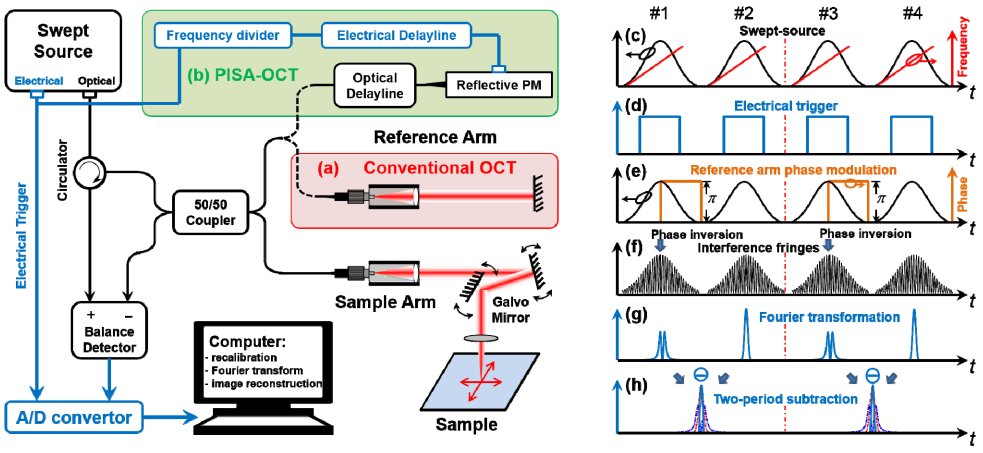

Fig. 1. Experimental setup of the conventional swept-source OCT (a) and the temporal phase modulation based PISA-OCT (b), and these two systems are almost identical except for the reference arm. (b) In the PISA-OCT, the mirror is replaced by a reflective phase modulator, and its driving signal is adjusted by a frequency divider and an electrical delay line. (c)-(h) Operation sequence of the temporal phase modulation scheme. (c) & (d) The swept-source and its electrical trigger in the temporal domain. (e) In the reference arm, the swept-source is phase modulated with a π-step in odd periods. (f) The interference fringes after combining the sample arm and reference arm, and the phase modulation will introduce a phase inversion for the odd periods. (g) After Fourier transformation, the single frequency peak becomes a twin-peak shape. (h) By subtracting these two neighboring periods, we can obtain sharper PSF. Here, the blue lines correspond to the electrical signals and the black lines correspond to the optical signals.

In a typical swept-source OCT system, the spatial depth difference between the sample and reference arms of a wideband source is encoded in the interference fringes in the spectral domain [Fig. 1]. This fast wideband swept-source is applied to temporally retrieve the wavelength information [20]; therefore, an ultrafast single pixel photodiode can obtain these wavelength fringes, which are required to retrieve the depth information [6]. The conventional reference arm provides a constant distance matching with the sample arm, and consists of a collimator and a mirror, as shown in Fig. 1(a). The axial resolving power is determined by the whole spectral bandwidth, which corresponds to the temporal NA, according to the analogy between the temporal tomography and the spatial microscopy [14]. Within limited spatial NA, some super-resolution microscope is achieved by manipulating its PSF, such as the STED microscopy. While for the swept-source OCT system, its PSF is the Fourier transform of the temporal interference fringes, thus this similar manipulation of the PSF can be performed in the time domain, such as the π-stepped temporal phase modulation, as shown in Fig. 1(b), where this reflective phase modulator is applied to replace the mirror, and it results in a twin-peak PSF. By subtracting this twin-peak PSF from the conventional Gaussian PSF, its sidelobe seems to be annihilated, thus we call this scheme phase-inverted sidelobe-annihilated OCT (PISA-OCT).

The temporal operation sequence of the PISA-OCT scheme is shown in Figs. 1(c)-1(h), which also illustrates the overall principle: there are four swept-source periods considered here, and the duty ratio of the electrical trigger is 50% [Fig. 1(d)], and all involved intensity profiles are a Gaussian shape. Figure 1(e) shows the phase modulation of the reference arm, and only the odd periods are manipulated, while the even terms are untouched. It is noted that, there is no extra arbitrary waveform generator (AWG) required for this temporal phase modulation, since it can be easily obtained from the electrical trigger, with a half-frequency divider and suitable electrical delay line as shown in Fig. 1(b). Therefore, after the tomography system, the interference fringes show the phase inversion in odd periods [Fig.

Optics EXPRESS

1(f)], and the corresponding Fourier transformation generates the twin-peak-shaped PSF, while that of the even periods remains a single Gaussian shape [Fig. 1(g)]. Finally, the PSF in the even period subtracts its preceding counterpart, and the resultant pulsewidth of the PSF is compressed [Fig. 1(h)]. Moreover, as long as the phase modulator is turned off, this system can be easily converted back to a conventional swept-source OCT system.

3. Results and discussion

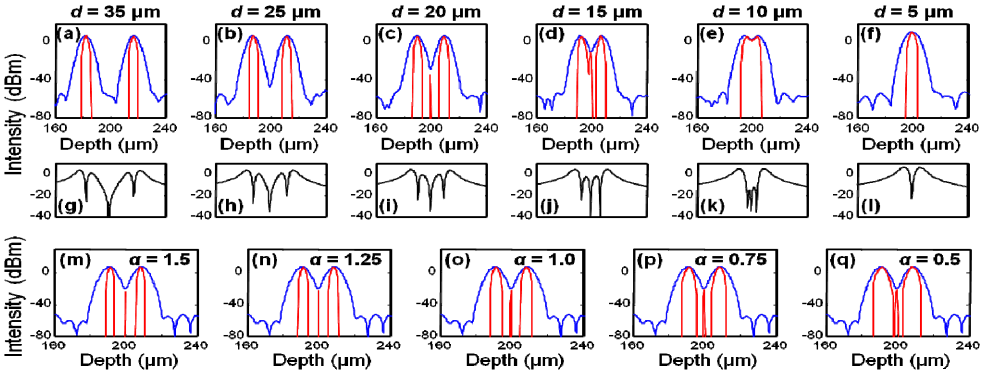

Fig. 2. Simulation study of the double-layer reflection characterization of the axial resolving power and the subtraction ratio. (a)-(f) The separation of these two layers is gradually tuned from 35 μm to 5 μm, and the subtraction ratio is kept at α = 1: the blue and red lines illustrate the resolving power of swept-source OCT and PISA-OCT, respectively. (g)-(l),The corresponding PSF shapes of the π-step phase-modulated periods. (m)-(q) The separation is maintained at 20 μm, and the subtraction ratio is gradually changed from 1.5 to 0.5: the blue and red lines illustrate the resolving power of swept-source OCT and PISA-OCT, respectively.

Manipulation of the PSF enables the STED microscope achieve super-resolution, and it is based on the fact that, the STED microscope is a point imaging system. From this point of view, the super-resolution scheme will not work for the tomography imaging, which is a line imaging system. However, the compression of the PSF will definitely improve the imaging quality, to quantify the resolution enhancement of a multi-layer sample, we first designed a double-layer simulation model with gradually changed separation, as shown in Figs. 2(a)-2(l). It is noticed that the PSF compression does not work when the separation is narrower than the axial resolving power of conventional OCT (d = 20 μm, Fig. 2(c)), which is twice that of the 3-dB resolution (R_{OCT} = 10 μm) [19]. In other words, PISA-OCT primarily improves the sharpness of the isolated layers, while its resolving power is still the same as conventional swept-source OCT, due to the affect of the adjacent layers; therefore, it cannot resolve density layers that cannot be resolved by swept-source OCT, as shown in Fig. 2(f). Another essential parameter of this subtraction strategy is the subtraction ratio α, which multiplies with the phase-modulated fringes before the subtraction, although it is a post-processing factor, and will not affect the practical data acquisition. Figures 2(m)-2(q) shows the simulation study by changing this ratio α. In general, a larger α achieves a sharper peak, while a smaller α maintains a larger effective region (see the appendix II document for detailed discussion) [21]. Therefore, α = 1 is usually selected to balance the performance, and it also helps to suppress the ghost fringes.

Optics EXPRESS

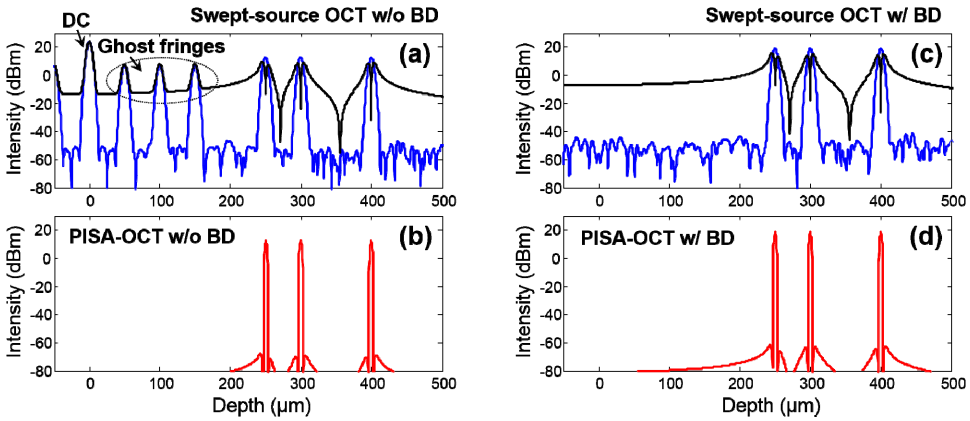

Fig. 3. Comparison of the swept-source OCT and PISA-OCT with/without balanced detection (BD). (a) & (c) the conventional swept-source OCT fringes in the frequency domain (blue lines), with/without BD. Black lines: the OCT fringes after the temporal phase modulation. (b) & (d) PISA-OCT fringes in the frequency domain (red lines), with/without BD.

In addition to the PSF compression, the autocorrelation term from the sample arm (ghost fringes) and direct current (DC) term can be suppressed by the PISA-OCT scheme, and the sensitivity is also improved with lower noise floor. Leveraging the aforementioned multi-layer simulation model, the swept-source OCT (blue lines) and PISA-OCT (red lines) are compared, with/without the BD, as shown in Fig. 3. It is interesting to notice that, the PISA-OCT scheme without BD [Fig. 3(b)] achieves similar suppression function as that of BD (blue line in Fig. 3(c)), where the DC and autocorrelation terms are fully suppressed (see appendix for detailed mathematic analysis). However, their performance in terms of sensitivity enhancement is slightly different: BD mainly increases the intensity power by 6 dB, while PISA-OCT mainly suppresses the background noise. Moreover, the PISA-OCT scheme is compatible with the BD, with the result shown in Fig. 3(d).

A stationary reflective mirror was first tested by PISA-OCT. In the ideal case, the precise frequency (namely position) is quantified by an infinitely long interference fringe; however, the limited spectral bandwidth of the swept-source confined the fringe temporal window to 20 μs (100-nm bandwidth at 50-kHz swept rate, as shown in Fig. 4(a)). Figure 4(b) illustrates the interference fringes of conventional swept-source OCT, or the un-modulated even periods. On the other hand, the π-step temporal phase modulation on the odd periods created the phase-inverted interference fringes [Fig. 4(c)], matching reasonably well with the ideal case in Fig. 1(f). Then, we performed Fourier transformation to generate the PSFs, which are shown as solid lines in Figs. 4(d) and 4(e) for conventional swept-source OCT and PISA-OCT, respectively. Their subtraction compressed the pulsewidth of the PSF from 20 μm to 4 μm, which corresponded to the axial resolution of the single layer (but differed from the axial resolving power, according to the aforementioned explanation). To quantify the observation range, the mirror was moved across the depth. Here, conventional swept-source OCT was measured to have a 4-mm depth range (–6-dB degradation by the roll-off curve in Fig. 4(f)). Since the peak value of conventional OCT overlaps with the trough of the twin-peak-shape, the subtraction will not change the peak value of the PSF; the roll-off curves of the two systems were almost identical, but a narrower pulsewidth of PSF and better signal-to-noise ratio (6-dB lower noise floor) were realized by PISA-OCT [Figs. 4(f) and 4(g)].

Optics EXPRESS

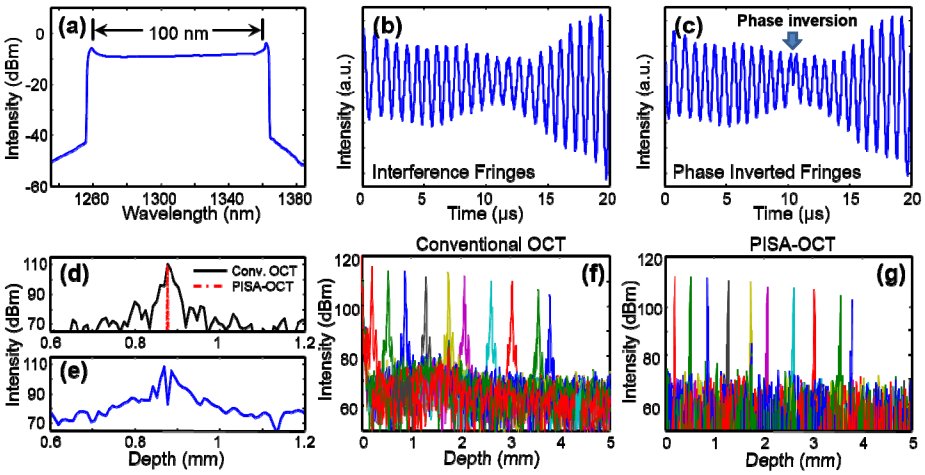

Fig. 4. Single layer reflection characterization of temporal phase modulation. (a) Spectrum of the swept-source (centered at 1310 nm, AXSUN Technologies, Inc.), with 100-nm bandwidth [20]. (b) & (c) The interference fringes for the odd/even periods with/without phase modulation respectively. (d) & (e) PSFs after Fourier transformation, conventional swept-source OCT (solid black line), compressed PISA-OCT (dash-dotted red line), and the phase-modulated two-peak PSF (solid blue line). (f) & (g) The roll-off measurement of conventional swept-source OCT (~1.5 dB/mm) versus PISA-OCT (~1.5 dB/mm).

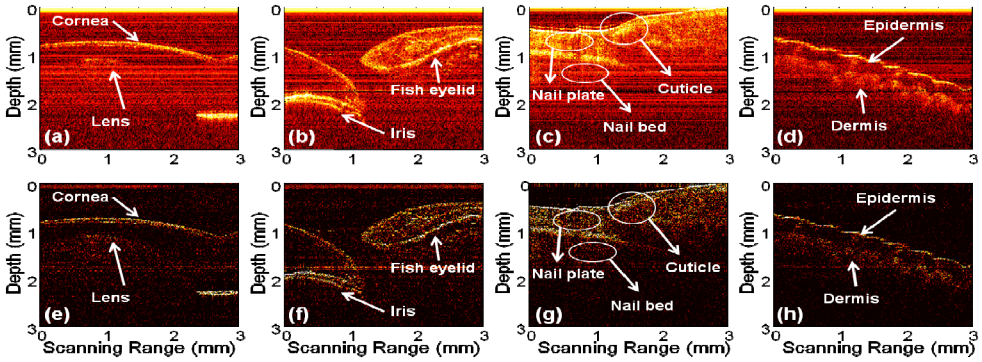

Fig. 5. Observation of the *in vivo* tomographic imaging improvement (without balanced detection). The top four figures are captured by swept-source OCT, and the corresponding bottom four figures are captured by PISA-OCT. (a) & (e), Cornea and lens of a fish eye. (b) & (f), Iris and eyelid of a fish eye. (c) & (g), Nail side of a human fingertip. (d) & (h), Fingerprint side of a human fingertip.

To demonstrate the improved imaging quality by PISA-OCT, we obtained images from a fish eye and a human fingertip. They were first measured by the swept-source OCT (without BD), which was implemented by simply turning off the phase modulation in the identical PISA-OCT setup [Fig. 1]. They were then measured by the PISA-OCT system (without BD) after the phase modulation was turned back on. Figures 5(a) and 5(e) show the images of the fish cornea and lens, respectively. It is clearly observed from Fig. 5(e) that the lens shape is recovered in PISA-OCT by suppressing ghost fringes and background noise. For the iris and eyelid, which have pronounced morphological information, axial resolution enhancement by PISA-OCT is clearly observable in Fig. 5(f), with narrower structural edging and lower background noise being achieved. Similar improvements also appear in the human fingertip measurement (Fig. 5(g): nail side and Fig. 5(h): fingerprint side), in which the sketch lines are compressed, and more information is recovered by suppressing the background noise.

Optics EXPRESS

4. Conclusion

We have presented, for the first time, the analogy between temporal tomography and spatial microscopy, based on space-time duality [14]. Temporal Fourier transformation can be optically performed at the focal plane of the time-lens, but most OCT techniques rely on digital transform to obtain the depth information, and the diffraction-limited resolution is determined by the spectral bandwidth [5,6,18]. Inspired by this space-time duality and the super-resolution STED microscope, where the PSF is greatly compressed by the depletion of a spatial phase modulated doughnut field. In this paper, we present an all-optical PSF manipulation scheme based on temporal phase modulation, though it will not directly improve the axial resolving power, since OCT is a line imaging system, the imaging quality can be enhanced by the well-defined single layer outlines. Moreover, this all-optical processing enables the real-time imaging. Owning to the 100-nm bandwidth limit, this PISA-OCT scheme compresses the isolated PSF from 20 μm to 4 μm, which means much sharper sketch lines can be obtained from the specimen. In addition to the sharper sketch lines, the autocorrelation term from the sample arm (ghost fringes) and direct current term can be suppressed by this scheme, and the sensitivity is also improved with lower noise floor. It is believed that the analogy between spatial microscopy and temporal tomography will shed light on the largely untapped super-resolution tomographic techniques, hence further contributing to the development of the optical imaging community.

Appendix I – Space-time duality between spatial microscopy and temporal tomography

Space-time duality was introduced to describe the analogy between the space-lens and the time-lens, and it can also be applied to microscopy and tomography. Table 1 lists the different parameters of the two systems and shows how these parameters correspond [14]:

Table 1. Space-time duality between spatial microscopy and temporal tomography.

Microscopy (spatial)		Tomography (temporal)	
Vertical axis	x, y	Time axis	t
Axial distance	z	GDD (dispersion)	Φ
Focal length	f	Focal GDD	Φ_f
Axial angle	θ	Wavelength	λ
Wavelength	λ	Group velocity	v_g
Numerical aperture	$D/2f$	Frequency bandwidth	$\Delta\lambda$

Previous research has demonstrated the analogy between the spatial diffraction and the temporal dispersion, and also the quadratic phase modulation between the space-lens and the time-lens, as shown in Table 1. In this paper, their Fourier transformation features were emphasized at the focal plane of these two systems. For the microscopy system, the spatial frequency (surface dimension) is focused as an intensity profile at the vertical axis, while in the tomography system; the temporal frequency (depth information) is focused as an intensity profile at the time axis. It is noted that most of the Fourier transformation in the tomography system was performed in the electrical domain, while the optical Fourier transformation based on the time-lens is highly desired [18].

Appendix II – Detailed mathematic model of the PISA-OCT

First, the swept-source needs to be modeled, assuming its intensity profile is a Gaussian shape, and its intensity and phase term need to be described separately

Optics EXPRESS

$$a(t) = A(t)\exp\left[i\phi(t)\right] = \exp\left[-2\ln 2\left(\frac{t}{T_0}\right)^2\right]\exp\left[i\frac{\Delta\omega}{2T_0}t^2 + i\omega_0 t\right] \quad (1)$$

where T_0 is the swept temporal window, and $\Delta\omega$ is the swept bandwidth. With a single layer reflection in the sample arm, this swept-source is delayed by $\delta t = 2\Delta d/c << T_0$. Therefore, the signal of the sample arm and the reference arm become

$$\begin{cases} a_s(t) = a(t-\delta t) \approx A(t)\exp\left[i\phi(t-\delta t)\right] \\ a_r(t) = ia(t) = iA(t)\exp\left[i\phi(t)\right] \end{cases} \quad (2)$$

where the imaginary unit of the reference arm is introduced by the π/2 phase shift of the 50/50 coupler, and thus the interference between the sample arm and the reference arm becomes (one port - constructive)

$$I_+(t) = \left|a_r(t) + ia_s(t)\right|^2 = 2\exp\left[-4\ln 2\left(\frac{t}{T_0}\right)^2\right]\left\{1+\cos\left[\frac{\Delta\omega\delta t}{T_0}\left(t-\frac{\delta t}{2}+\frac{\omega_0 T_0}{\Delta\omega}\right)\right]\right\} \quad (3)$$

The Fourier transformation of this intensity trace can be described by

$$\begin{aligned} D(\omega) &= \left|F\left[I(t)\right]\right| \\ &= \sqrt{\frac{\pi}{\ln 2}}T_0\left\{\frac{1}{2}\exp\left[-\frac{T_0^2}{16\ln 2}\left(\omega-\frac{\Delta\omega\delta t}{T_0}\right)^2\right]+\frac{1}{2}\exp\left[-\frac{T_0^2}{16\ln 2}\left(\omega+\frac{\Delta\omega\delta t}{T_0}\right)^2\right]+\exp\left[-\frac{T_0^2\omega^2}{16\ln 2}\right]\right\} \end{aligned} \quad (4)$$

By applying the frequency-to-depth relation $\omega = 2\Delta\omega d/cT_0$, the depth information becomes:

$$D(d) = \sqrt{\frac{\pi}{\ln 2}}T_0\left\{\frac{1}{2}\exp\left[-\frac{\Delta\omega^2}{c^2 4\ln 2}(d-\Delta d)^2\right]+\frac{1}{2}\exp\left[-\frac{\Delta\omega^2}{c^2 4\ln 2}(d+\Delta d)^2\right]+\exp\left[-\frac{\Delta\omega^2 d^2}{c^2 4\ln 2}\right]\right\} \quad (5)$$

From Eq. (5), we can obtain the axial resolution $R_{OCT} = 2\ln 2\lambda^2/\pi\Delta\lambda$; this is limited by the spectral bandwidth and wavelength, which is quite similar to the diffraction limit of the aforementioned microscopy. Therefore, to break through the limited resolution, schemes that are similar to those in the STED microscope may be applicable to the tomography system. First, we introduce a temporal phase mask (namely a phase modulator) in the reference arm, and the signals of the sample arm and the reference arm become

$$\begin{cases} a_s(t) = a(t-\delta t) \approx A(t)\exp\left[i\phi(t-\delta t)\right] \\ a_r(t) = ia(t)\,\mathrm{sgn}(t) \approx iA(t)\exp\left[i\phi(t)\right]\mathrm{sgn}(t) \end{cases} \quad (6)$$

The interference fringes of one port thus become

$$I_+'(t) = \left|a_r(t) + ia_s(t)\right|^2 = 2\exp\left[-4\ln 2\left(\frac{t}{T_0}\right)^2\right]\left\{1+\cos\left[\frac{\Delta\omega\delta t}{T_0}\left(t-\frac{\delta t}{2}+\frac{\omega_0 T_0}{\Delta\omega}\right)\right]\mathrm{sgn}(t)\right\} \quad (7)$$

The Fourier transformation of this intensity trace can be described by

$$\begin{aligned} D'(\omega) &= \left|F\left[I'(t)\right]\right| \\ &= \sqrt{\frac{\pi}{\ln 2}}T_0\left\{\exp\left(-\frac{T_0^2\omega^2}{16\ln 2}\right)+\sqrt{2}\left|D_+\left[\frac{T_0}{4\sqrt{\ln 2}}\left(\omega-\frac{\Delta\omega\delta t}{T_0}\right)\right]\right|+\sqrt{2}\left|D_+\left[\frac{T_0}{4\sqrt{\ln 2}}\left(\omega+\frac{\Delta\omega\delta t}{T_0}\right)\right]\right|\right\} \end{aligned} \quad (8)$$

Similarly, $D_+(x) = \exp(-x^2)\int_0^x \exp(t^2)dt$ is the Dawson function. Also, if the frequency-to-depth relation $\omega = 2\Delta\omega d/cT_0$ is applied, the depth information becomes

Optics EXPRESS

$$D'(d)=\sqrt{\frac{\pi}{\ln 2}}T_0\left\{\exp\left(-\frac{\Delta\omega^2 d^2}{4c^2\ln 2}\right)+\sqrt{2}\left|D_+\left[\frac{\Delta\omega(d-\Delta d)}{2c\sqrt{\ln 2}}\right]\right|+\sqrt{2}\left|D_+\left[\frac{\Delta\omega(d-\Delta d)}{2c\sqrt{\ln 2}}\right]\right|\right\} \quad (9)$$

There are two symmetric twin-peak structures in the frequency domain, namely the modulated interference peak and the central peak, which is the DC component. Unlike with STED microscopy, there is no stimulated emission depletion to perform the subtraction. Therefore, these two traces [Eq. (5) and Eq. (9)] are obtained separately, and the enhanced tomography trace is their subtraction as follows:

$$\begin{aligned} D''(d) &= D(d)-D'(d) \\ &= \sqrt{\frac{\pi}{\ln 2}}T_0\left\{\frac{1}{2}\exp\left[-\frac{\Delta\omega^2}{4c^2\ln 2}(d-\Delta d)^2\right]-\sqrt{2}\left|D_+\left[\frac{\Delta\omega(d-\Delta d)}{2c\sqrt{\ln 2}}\right]\right|\right\} \\ &+\sqrt{\frac{\pi}{\ln 2}}T_0\left\{\frac{1}{2}\exp\left[-\frac{\Delta\omega^2}{4c^2\ln 2}(d+\Delta d)^2\right]-\sqrt{2}\left|D_+\left[\frac{\Delta\omega(d+\Delta d)}{2c\sqrt{\ln 2}}\right]\right|\right\} \end{aligned} \quad (10)$$

The central DC components are identical, and are thus removed after subtraction.

Funding

Research Grants Council of the Hong Kong Special Administrative Region, China (Project Nos. HKU 17208414, HKU 17205215, CityU T42-103/16-N, and E-HKU701/17); National Natural Science Foundation of China (NSFC) (61735006, 61675081, and 61505060); NSFC/RGC Joint Research Scheme (N_HKU712/16 and 61631166003); GD-HK Technology Cooperation Funding Scheme (GHP/050/14GD); Director Fund of WNLO.